SANDIA REPORT

SAND91-2202 • UC-237
Unlimited Release
Printed December 1991

Testing of the Prototype Facets for the Stretched-Membrane Faceted Dish

J. W. Grossman, R. M. Houser, W. W. Erdman

Prepared by
Sandia National Laboratories
Albuquerque, New Mexico 87185 and Livermore, California 94550
for the United States Department of Energy
under Contract DE-AC04-76DP00789

Printed in the United States of America. This report has been reproduced directly from the best available copy.

Available to DOE and DOE contractors from
Office of Scientific and Technical Information
PO Box 62
Oak Ridge, TN 37831

Prices available from (615) 576-8401, FTS 626-8401

Available to the public from
National Technical Information Service
US Department of Commerce
5285 Port Royal Rd
Springfield, VA 22161

NTIS price codes
Printed copy: A02
Microfiche copy: A01

Distribution
Category UC-237

SAND91-2202
Unlimited Release
Printed December 1991

TESTING OF THE PROTOTYPE FACETS FOR THE STRETCHED-MEMBRANE FACETED DISH

J. W. Grossman, R. M. Houser, and W. W. Erdman
Divisions 6216 and 6215
Sandia National Laboratories
Albuquerque, New Mexico 87185

Abstract

The Faceted Stretched-Membrane Dish Program is part of a DOE-sponsored effort to develop a commercial 25 kW_e dish/Stirling system employing a twelve-facet dish concentrator. The facets will utilize the stretched-membrane technology originated in the heliostat development program. Each facet is constructed with a thin metal membrane stretched over both sides of a steel ring. When a small vacuum is induced between the membranes they assume a parabolic contour capable of concentrating sunlight at a predetermined focal length. A reflective polymer film is attached to the face of the facet to enhance the optical performance.

During Phase II of the Faceted Stretched-Membrane Dish Program, Science Applications International Corp. and Solar Kinetics, Inc., constructed prototype 3.5-meter facets utilizing different design approaches to demonstrate their manufacturability and optical performance. Sandia engaged in a program to determine the on-sun performance of the facets (for f/Ds of 2.7 to 3.0). A uniformly distributed slope error was used as the basis for comparison. Flux arrays based on slope error from a computer model were compared to a measured flux array for each facet. The slope error for the facet was determined by the value that would produce a modeled array with the minimum mean square difference to the measured array. The facet produced by SAIC demonstrated uniform slope errors of 2.2 to 3.0 milliradians with peak flux intesities of 334 to 416 kW/m^2. The SKI facet had slope errors of 1.6 to 1.9 milliradians with peak flux intesities of 543 to 1186 kW/m^2.

1. Introduction

1.1 Test Facility

The National Solar Thermal Test Facility (NSTTF) [1,2] is operated by Sandia National Laboratories for the U. S. Department of Energy's Solar Thermal Program. The NSTTF, located on Kirtland Air Force Base in Albuquerque, NM, is capable of supporting a wide range of solar experiments. Data acquisition, control and diagnostic systems are available for the use of the experimenter. In addition, specialized instrumentation such as the Beam Characterization System (BCS), used to measure the solar intensity profiles produced by all types of concentrators, has been developed at the NSTTF. Sandia has also developed several computer codes, HELIOS [3] and CIRCE[4] and CIRCE2 [5], to model solar concentrator and receiver optical performance. Incorporated in the analysis of the results is a methodology for analytically comparing the real image measurements with the theoretical predictions, and it enhances our ability to predict receiver performance.

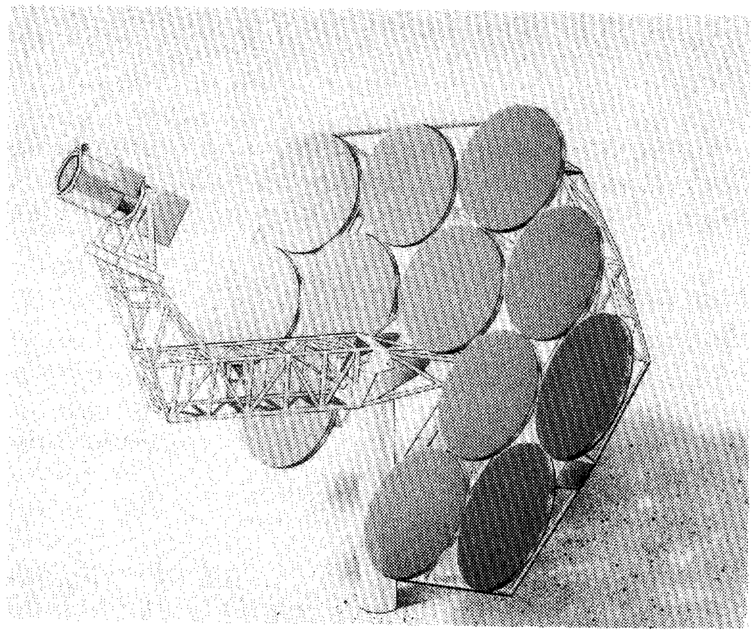

Figure 1. Stretched-Membrane Faceted Dish Conceptual Drawing.

1.2 Faceted Stretched-Membrane Dish Program

The goal of the Faceted Stretched-Membrane Dish Program is to develop a 25 kW_e modular dish/Stirling power-production system. The stretched-membrane facets are similar in concept to the stretched-membrane heliostat. In general, the facets are made by attaching tensioned metal membranes to a steel support ring. One of the membranes has a reflective surface on the exposed face. When a small vacuum is drawn on the inside of the structure, the membranes assume a concave shape, and the reflective surface acts as a focusing mirror. One design discussed in this report applies a different approach, employing a plastically deformed front membrane. Twelve of the facets will be mounted on a space frame to form a parabolic concentrator, as shown in Figure 1. The design goal for the facet uniform slope error is 2.5-mr (1 standard deviation)[6].

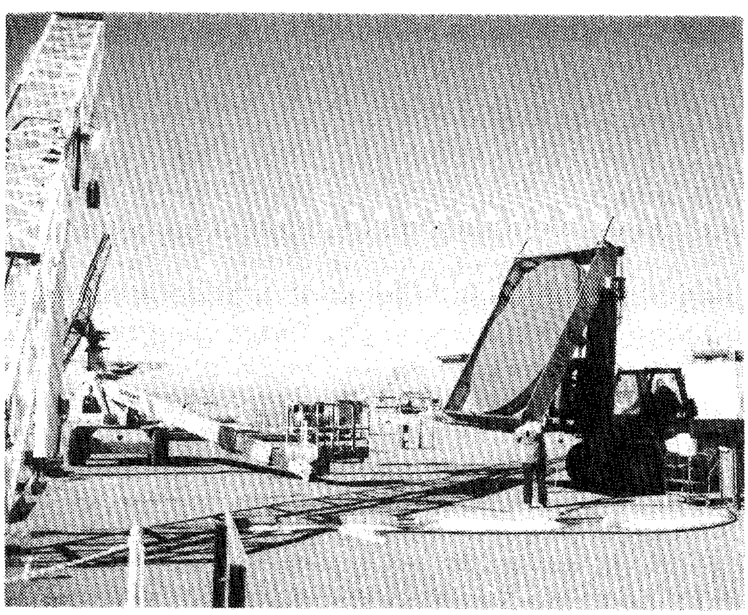

Figure 2 On-Sun Testing of a Stretched-Membrane Facet

As part of the program, two contractors, Science Applications International Corp. (SAIC)[7] and Solar Kinetics, Inc., (SKI)[8] fabricated prototype 3.5-m. diameter facets that were tested on-sun at the NSTTF (Figure 2.). This report summarizes the testing and analysis done in connection with this phase of the program.

2. Test Facets

2.1 The SAIC Facet

The membrane for the facet supplied by SAIC was fabricated from 0.076-mm thick, Type 201, half-hard stainless steel. The membranes are pre-tensioned and then welded to the facet ring. The front membrane has a laminated reflective surface of silvered EPC 305, a 3M company product. Aluminized EPC 244 tape was used to seal the exposed seams of the laminate. Focusing of the SAIC facet is achieved by providing a vacuum in the space between the membranes. The membranes deflect inward until the front one contacts the internal focus control valve and shuts off the vacuum. The deflections of the front membrane from the ring plane necessary to meet the required focal lengths were supplied by SAIC (Table 1). The position of the focus control valve was adjusted until the proper displacement was measured at the center of the front membrane.

Table 1
SAIC Front Membrane Displacement

Focal Length m	Displacement mm
9.5	83.4
10.0	79.9
10.5	75.0

2.2 The SKI Facet

SKI uses a different approach in fabricating its prototype facet. The front membrane is plastically deformed during fabrication to a contour that approximates a parabola. The front membrane of the prototype is 0.08-mm thick 304 stainless steel. The reflective film laminated on the front membrane is EPC 305. The rear membrane is a 304 stainless steel membrane 0.10-mm thick. At the center of the facet, a tether is installed between the membranes to stabilize the thin front surface in winds. The membranes are held to the ring assembly with spring clips.

To focus the facet, a pressure difference is maintained between the front face of the facet and the interior. A pressure controller is used to cycle a vacuum pump to sustain the prescribed differential. Set points for the controller (Table 2) were provided by SKI.

Table 2
SKI Differential Set Point

Focal Length m	Set Point in. of water
9.5	3.95
10.0	3.20
10.5	2.45

3. Test Equipment and Configuration

3.1. Beam Characterization System

The test instrumentation used to measure the on-sun flux density distributions produced by concentrators is Sandia's Beam Characterization System (BCS). A schematic diagram of the system is shown in Figure 3. The BCS comprises a lambertian target plane with an internal flux gauge, a video camera with neutral density filters, and a computer system with a frame grabber that digitizes the video image, displays it on a monitor and stores it for later evaluation. The digitized image is processed with a software package called Beamcode© (enhanced for Sandia by the developer Big Sky Software) to provide flux contours, total beam power, and the flux-density distributions.

The solar image from the concentrator is reflected onto a water-cooled target with a plasma-sprayed aluminium oxide coating. Previous laboratory measurements of these surfaces have shown them to be nearly lambertian [9]. Flux gauges are located at two points in the target surface, providing a direct measurement of the flux density at their location within the reflected flux-density profile so that the measured gray-scale level can be scaled and equated with a solar intensity. The flux gauge configuration is a water-cooled circular foil heat flux gauge.

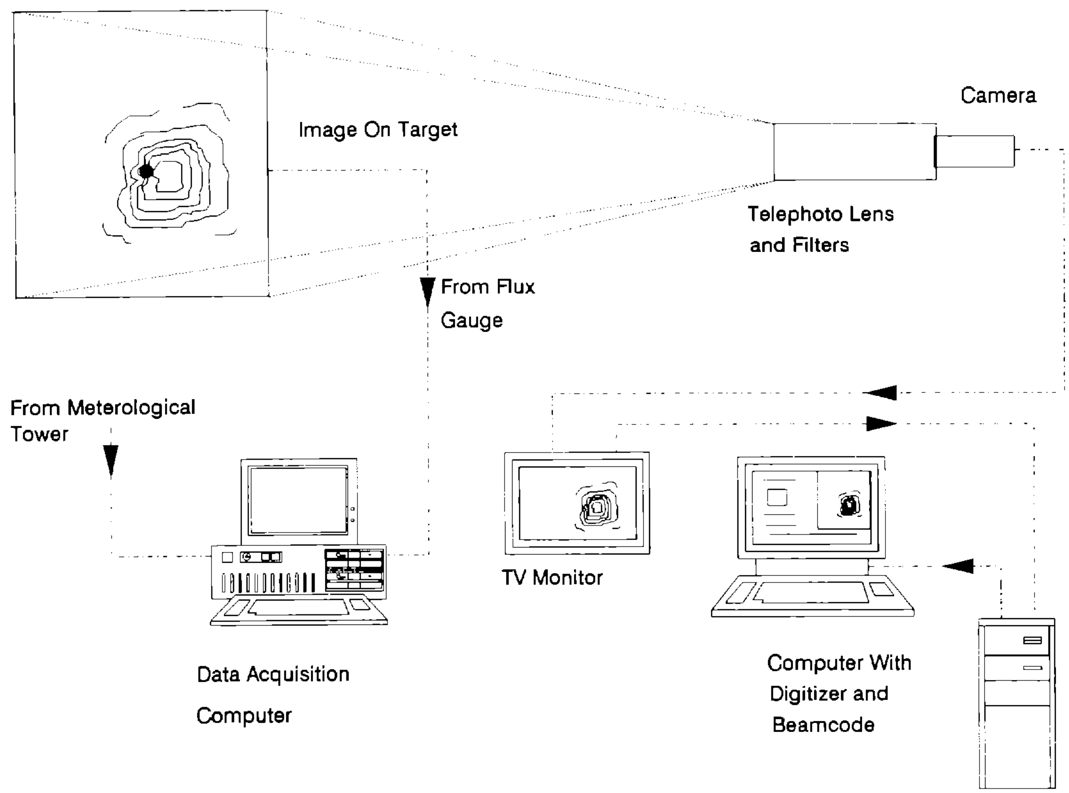

Figure 3. Beam Characterization System Schematic

A video camera is used to view the reflected image at the receiver plane. The camera has a visual spectral response, a wide dynamic range, high resolution, zero geometric distortion, and no lag or image retention. Standard "C" mount lenses with neutral density filters are used on the camera to adjust the intensity levels viewed by the camera to avoid saturation. The video frame grabber and digitizer provides a spatial resolution up to 240 by 240 pixels with 256 grey-scale intensity levels. Images can be captured at rates up to 60 per second.

3.2 Test Configuration

Both facets were delivered to Sandia mounted in shipping containers that also served as the facet support structure. A mounting frame for the containers was built at the NSTTF that could hold the facet at an angle on a fork lift. The fork lift used for positioning the facets has the capability for six directions of motion (up-down, forward-backward, left-right, tilt, pan, and rotation). A tarp sized to cover most of the face of the facets was fixed to the frame so it could be raised and lowered to shield the facets from the sun when focusing of the sun was not desired.

A water-cooled target with flux gauges was mounted at a fixed position in an open area of the test site. A measurement grid was surveyed and marked on the asphalt north of the target. The facets were positioned on the grid with the fork lift so that the concentrated beam struck the target. The BCS camera was positioned adjacent to the facet to record the images. Figure 4 is a schematic of the test configuration.

3.3 Uncertainties In The Measurements

The uncertainties in the measurements made during on-sun testing are listed in Table 3. The most important reduced measurement made in these tests is the scale factor that was developed to establish the flux levels associated with the measured flux-density distributions. This measurement is the first uncertainty in the chain of measurements that leads to a flux uncertainty. Also part of this chain is the uniformity of the neutral density filters, the correction for the angle between the camera view and the target normal, and the uncertainty in the size and intensity of a pixel in the final distribution. Our estimate is that the measured flux-densities are within ± 8% of the reported peak-flux value.

4. Test Procedure

For each test, the focus control was set according to the instructions supplied by the facet fabricator. The covered facet was positioned with the fork lift on the grid so that the reflected beam was striking the target. With the tarp lowered, enough of the sides of the facet were uncovered to allow initial positioning of the facet.

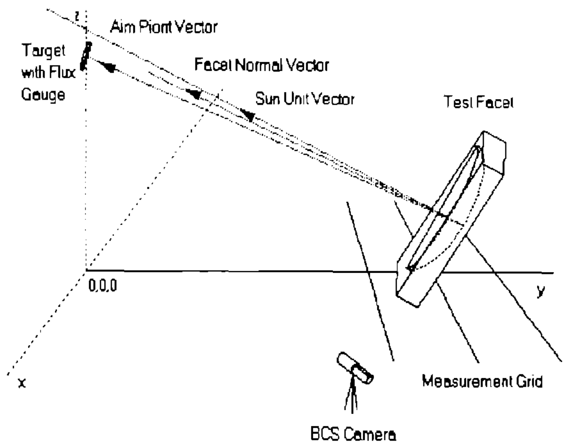

Figure 4. Stretched-Membrane Facet Test CIRCE2 Configuration

Measurements from the bottom edge of the facet mounting frame to the grid provided input to calculations to determine the vertex to target distance and azimuth angle. The facet position was adjusted until the calculated distance was close to the desired focal length, and the facet was uncovered to allow capture of a series of BCS images. This process was repeated for both facets at each focal length. The second and third columns of Table 4 show the desired (design) and the actual (test) focal lengths. Details of the calculations are in Appendix 1.

The object of these tests was to measure the optical performance of the facets at fixed focal lengths corresponding to the positions of the facets on the dish. The test setup did not have any automatic sun-tracking capability. The facets were manually positioned for each test, and the procedure was not intended to bracket the focal point or determine the optimal focal length. Since the completion of these tests, a test apparatus equipped with sun tracking and a movable target has been developed and will be used to test the next generation of facets.

5. Test Results

The images captured with the BCS were analyzed to determine peak flux and image shape. Peak flux results are listed in the fourth column of Table 4. Flux values reported by Beamcode© are relative to the zero background of the image. As part of the test procedure for the BCS, a nonilluminated image of the target is made prior to the actual test sequence. This image is subtracted from each test image by the software as a means of reducing "background noise." As a result, each pixel in the digitized test image has an integer value of 0 to 255 relative to the 0 pixel level. Actual flux values are determined using the flux gauge measurements and

Table 3
Measurement Uncertainties

Measurement Variable	Measured Uncertainty
Time of Day	± 5 Seconds
Ambient Temperature	± 0.28 ° C
Wind Speed	± 5 % of reading
Wind Direction	± 10 % of reading
Solar Radiation	± 2 % of reading
Target Flux	± 8 % of maximum value
Target-to-Facet Distance	± 0.03 m
Azimuth and Elevation angles	± 0.5 Degrees
Reflectivity	± 2 % of reading

are normalized to 1 kW/m². Flux gauge locations in the target appear as holes in the image surface. Viewing profiles of the hole with the software provide a means for gauging the relative intensity of the pixels at the edge of the gauge location. By interpolation, a relative intensity for the pixel located at the center of the gauge can be determined. This pixel value is ratioed with the measured flux from the gauge to determine the intensity scale factor (kW/m²/pixel relative intensity) for the entire image array. The peak flux values are the average of the scale factor for each flux gauge times the peak pixel relative intensity of the image. The power (fifth column Table 4) is determined by multiplying the sum of the image array by the intensity scale factor and the amount of the target area in one pixel.

Table 4
Stretched-Membrane Facet Test Results

Test Number	Design Focal Length m	Test Focal Length m	Peak Flux kW/m²	Power kW
SAIC				
H0121144	10.5	10.7	416	8.50
H0121213	10.5	10.5	338	8.79
H0121224	10.5	10.6	389	9.33
H0151209	10.0	10	342	8.68
H0151223	10.0	10.1	357	8.71
H0151232	10.0	10.0	339	8.59
H0231122	9.5	9.6	355	8.92
H0231136	9.5	9.5	334	9.20
H0231148	9.5	9.6	346	8.92
H0231201	9.5	9.6	347	9.12
H0231210	9.5	9.7	365	9.16
H0231218	9.5	9.7	368	9.04
SKI				
H0251155	10.5	10.4	784	9.17
H0251205	10.5	10.6	798	9.16
H0251212	10.5	10.6	843	9.52
H0251220	10.5	10.6	638	9.21
H0251228	10.5	10.7	797	9.57
H0281129	10.0	10.1	1163	8.53
H0301145	10.0	10.3	1090	8.54
H0301154	10.0	10.0	1186	9.08
H0301208	9.5	9.6	543	7.95
H0301218	9.5	9.5	755	7.99
H0311031	9.5	9.8	645	6.19
H0311039	9.5	10.0	921	8.82
H0311121	9.5	10.0	1182	8.86

During testing, some problems were encountered with the focusing system for the SKI facet. Covering and uncovering the facet with the tarp caused large pressure fluctuations that the control system could not accommodate. While the test conditions could have exaggerated the pressure changes,whenever cloud transients occur they may also induce pressure changes which might affect the control system. In addition, while the prescribed vacuum differential for the 9.5-m focal length could be maintained, the actual focal length could not be established. The vertex-to-target distance was varied while using the BCS to determine the beam size. The smallest diameter image corresponded to a vertex-to-center distance of 9.9 m. The measured peak flux (1182 kW/m²) was also consistent with the values measured at 10 m. This would indicate that the change in vacuum did not cause a corresponding change in focal length or facet contour, and the decrease in peak power at the 9.5-m. focal length was a function of the movement away from the 10-m. focal point.

6. Test Analysis

6.1 The CIRCE2 Computer Code

CIRCE2 is a dish/receiver- specific code adapted from HELIOS, a code developed in the late 1970's for central receiver systems (in Greek mythology Circe is the daughter of Helios). The solution technique employed in CIRCE2 is the same as in HELIOS; that is, the concentrator errors are convolved with the sunshape to produce the flux density distribution on an arbitrary target plane.

6.2 CIRCE2 Input

Input to CIRCE2 is a file containing the parameters listed below arranged in a specific sequence. A short program creates the file and prompts the user for the required input.

Sunshape

The sunshape input can be either Gaussian, a uniform disk with any of six limb-darkening options, or a user-specified tabular input. A clear-day, tabular sunshape, measured at the NSTTF, was used for these calculations.

Sun, Dish, and Target Orientation

In CIRCE2, the default position of the sun is directly overhead of an upward facing dish. Inputs to the program allow for specification of the position vectors for the sun, the target, and the concentrator. By transforming the test coordinate system to CIRCE2 coordinates, the program inputs model the actual positions of the sun, target and concentrator. Appendix 1 details the calculations for determining the position inputs to CIRCE2.

Error Parameters

Up to five different reflector errors can be input to the code as either one-dimensional (circular normal) or two-dimensional (elliptic normal) errors. A single, circular-normal slope error was used to model the performance of the facets. The slope error is input to the code to model flux distribution. The slope error is varied until predicted peak flux closely matches the measured peak flux. This match is determined when a 0.1 change in the slope error determines flux values that bracket the measured flux value.

Convolution

The convolution of the errors and the sunshape can be one- or two-dimensional and either numerically or analytically calculated. A two-dimensional numerical convolution is used for the concentrators because of the offsets and the tabular sun input.

Target Shadowing

Target shadowing or blockage of the reflective surface can be input as a percentage of the concentrator projected area, or computed internally by overlaying a projection of the target on the facets. Target shadowing is neglected in these tests since no shadowing occurred.

Reflector Types

CIRCE2 can model either continuous surfaces or faceted concentrators. The reflectance of the optical surface is also an input variable. The facets were modeled as continuous surfaces, and the measured solar reflectivity was input to the models.

Facet Shape

CIRCE can support a number of different reflector shapes. For these calculations, circular was used.

Facet Contour

The facet contours were modeled as parabolic.

6.3 CIRCE2 Slope Error

The CIRCE2 code models the facet as a contour of revolution; that is, the reflector surface is axisymmetric. The primary assumption in the code is that the slope errors are uniformly distributed over the surface of the reflector. In fact, this is rarely the case since fabrication techniques often result in organized departures of the facet contour from design. Nonetheless, the uniformly distributed slope error used in CIRCE2 is useful as a figure-of-merit for comparing the relative performance of the facets.

6.4. Comparing Images

One method for using CIRCE2 and the BCS for analyzing test results has been to vary the uniform slope error in CIRCE2 until the peak flux determined by the code closely matches the value ascertained from the image data. The BCS software allows input of a factor to scale the image to the actual peak flux and includes some functions to provide graphical and digital information. However, the size of the files is much larger than the 25 by 25 flux intensity array generated by CIRCE2, so visual comparisons of the image contours or profiles for analysis have been the general practice. This is a fairly subjective method, which uses uniform slope error as a figure-of-merit usually reported with two significant digits.

A second more rigorous comparison method has been applied to the analysis. The comparison begins by converting the binary image data file, which represents the entire viewing area of the digitizer, to a 240 by 240 array of real intensities. The actual beam image is only a portion of this array. The BCS software is used to locate the centroid of the image, determine the size of the pixels, and define a rectangular aperture enclosing the image. This information can be used to extract a 25 by 25 flux intensity array which is directly comparable to the CIRCE2 generated array.

The dimensions of the aperture used to extract the actual image array are used as the input for the target dimensions in CIRCE2 . The slope error determined by the code that matches the peak power of the image data is used as the starting point for a series of additional CIRCE2 runs. In each run (a minimum of four are done), the slope error is varied by half a milliradian. The series is determined so that the starting slope error is not one of the endpoints of the series.

The flux intensity arrays calculated in the series are put into a spreadsheet along with the extracted measured intensity array. Each array is normalized by its maximum value. For each slope error increment, an array of the differences between the measured and calculated values is created. A statistical figure-of- merit for the goodness of the fit is then calculated by computing the square root of the sum of squares (RSS) of the elements in each difference array.

7. Analysis Results

One set of tests results for both facets at each focal length was analyzed with CIRCE2. The facet location measurements were used to calculate facet normal and aim point vectors for input into the program (see Appendix 1). Sun position was determined from the time and date. The coordinate system used is shown in Figure 4.

The procedure used in the analysis began with a slope error determination based on peak power. This provided a starting point for calculating 0.5 mr interval arrays for use in the RSS difference. For each test, a graph of these RSS differences versus slope error was used to determine the calculated slope error with the least RSS difference. Figure 5 is an example of these graphs. The data shown is for the SAIC facet at the 10-m focal length (test #H0151223). The data is contained in Appendix 2 and includes these curves as well as contour plots of the actual image and the CIRCE2 output. A fourth order poynomial curve fit is used to generate the line connecting the data points. The analysis results are summarized in Table 5. Included with the results are uniform slope errors measured at the National Renewable Energy Laboratory (NREL formerly SERI) prior to the Sandia tests using the SHOT [10] system. The SHOT measurements were made under laboratory conditions using a laser ray trace system. Figure 6 shows the RSS difference results compared with

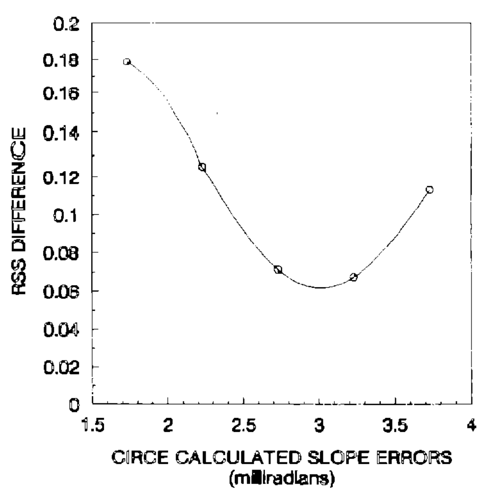

Figure 5 RSS Difference

Table 5.
CIRCE2 And SHOT Results For The Stretched-Membrane Facets

Test #	Focal Length (m)	Peak Flux Matching Slope Error (mr)	RSS Difference Slope Error (mr)	SHOT Slope Error (mr) (Focal Length)
SAIC				
H0121144	10.5	2.2	2.2	2.6(10.45)
H0151223	10.0	2.8	3.0	2.7(9.9)
H0231218	9.5	2.8	3.0	2.8 (9.6)
SKI				
H0251212	10.5	1.5	1.6	1.5 (10.45)
H0301154	10.0	1.3	1.2	1.2 (9.9)
H0301218	9.5	2.0	1.9	1.3 (9.6)

the SHOT measurements. The close agreement between these completely independent measurements reinforces the validity of all the results as they apply to these facets.

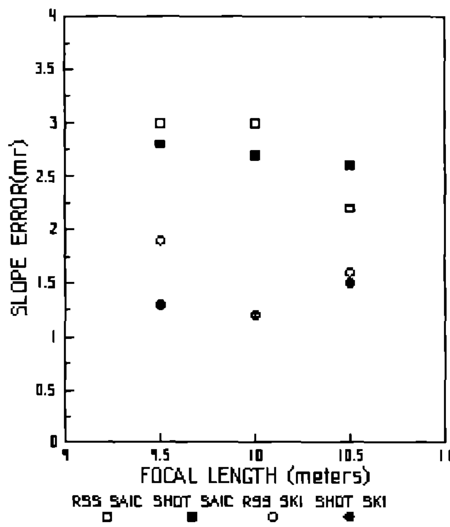

Figure 6 Comparison of RSS Difference SHOT Slope Errors

8. Conclusions

1. Slope errors for the SAIC facet are slightly higher than the design goal of 2.5 mr and are considered acceptable for this stage of the project. The focus control system functions properly and maintains set point.

2. The SKI facet slope errors surpass the design goal for optical performance. However, the focus control system did not perform in a completely predictable manner and requires more development.

3. The on-sun slope error results agree well with independent measurements made with SHOT.

The results of the analysis indicate that, for prototypes, both designs did well and are approaching, if not already capable of meeting, the design goal for optical performance. Both facets are still in the development stage and the lessons learned during these tests will help improve the final designs.

9. References

1. Maxwell, C. W., and J. T. Holmes, *Central Receiver Test Facility Experiment Manual*, SAND 86-1492, Sandia

National Laboratories, Albuquerque,NM, Reprinted March 1988.

2. *National Solar Thermal Test Facility*, SAND 89-1691, Sandia National Laboratories, Albuquerque, NM, 1989.

3. Biggs, F., and C. N. Vittitoe, *The HELIOS Model for the Optical Behavior of Reflecting Solar Concentrators,*SAND 76-0347, Sandia National Laboratories, Albuquerque, NM, March 1979.

4. Ratzel, A. C.,and B. D. Boughton, *CIRCE.001:A Computer Code for Analysis of Point-Focus Concentrators with Flat Target*, SAND 86-1866, Sandia National Laboratories, Albuquerque, NM,February 1987.

5. Romero, V. J., *CIRCE.2:/DEKGEN2::A Software Package for Facilitated Optical Analysis of 3-D Distributed Solar Energy Concentrators - Theory and Users Manual*, SAND 91-2238, Sandia National Laboratories, Albuquerque, NM, to be published.

6. "Statement of Work Faceted Stretched-Membrane Dish Development Project," Sandia Contract No. 42-9814, Sandia National Laboratories, June 7, 1989.

7. *Facet Development for a Faceted Stretched-Membrane Dish by SAIC.*, SAND 91-7008 (Science Applications International Corp.), Sandia National Laboratories, Albuquerque, NM, to be published.

8. *Facet Development for a Faceted Stretched-Membrane Dish by Solar Kinetics, Inc.*, SAND 91-7009 (Solar Kinetics, Inc., Dallas, Texas), Sandia National Laboratories, Albuquerque, NM, March 1989.

9. Mahoney, A. R., Sandia National Laboratories, Albuquerque, New Mexico, Memo to W.W. Erdman, September 12, 1991.

10 Wendelin, T. J., G. L. Jorgensen, and R. L. Wood, *SHOT: A Method for Characterizing the Surface Figure and Optical Performance of Point Focus Solar Concentrators*, presented at the Second ASME-JSES-JSME International Solar Energy Conference, Reno, Nevada, March 1991.

10. Appendices

Appendix 1
Equations

Determining Vertex to Target Distance

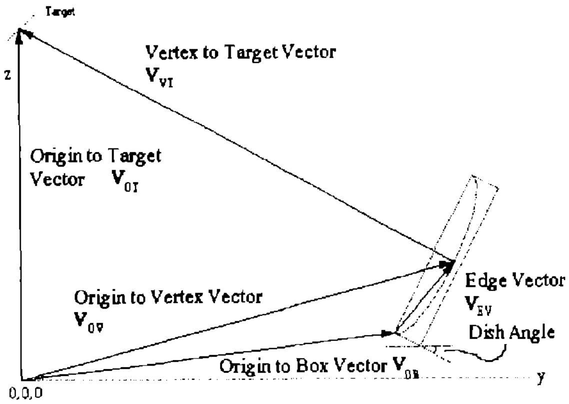

$$|V_{VT}|^2 = |V_{OT}|^2 + |V_{OV}|^2 - 2|V_{OT}|*|V_{OV}|\cos(\theta)$$

where :

$$|V_{OT}|*|V_{OV}|\cos(\theta) = V_{OT} \bullet V_{OV}$$

and

$$V_{OT} = V_{OB} + V_{EV}$$

Grid Layout Centerpoint Dimensions (Distance From Origin)

Centerpoint	x_{Ln}	y_{Ln}	z_{Ln}
First Line L1	0	7.94 m	-0.21 m
Second Line L2	0	8.39 m	-0.21 m
Third Line L3	0	8.85 m	-0.21 m

During testing, distances were measured from the box edge(center and corners) to the centerpoint of:

L1 for the 9.5-m focal length (center coordinates x_1, y_1, z_1).

L2 for the 10.0-m focal length (center coordinates x_2, y_2, z_3).

L3 for the 10.5-m focal length (center coordinates x_3, y_3, z_3).

The Origin to Box Vector V_{OB} is determined by adding the grid dimensions to the measured distances:

$$V_{OB} = (X_n + X_{Ln}) + (Y_n + Y_{Ln}) + (Z_n + Z_{Ln})$$

The Edge Vector V_{EV} is determined from the test facet dimensions and the Dish Angle (measured with a clinometer before each test):

Side View - Test Facet

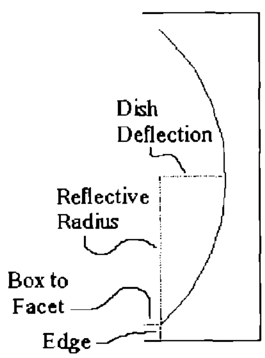

Test Facet Dimensions

Dimension	SAIC	SKI
Dish Deflection	meters	meters (vacuum in water)
@ 9.5-m	0.0833	0.0833 (3.95)
@ 10.0-m	0.0800	0.0818 (3.2)
@ 10.5-m	0.0751	0.0781 (2.54)
Reflective Radius	1.861	1.814
Box to Facet	0.109	0.044
Edge	0.134	0.206

$$\mathbf{V}_{EV} = \mathbf{X}_{EV} + \mathbf{Y}_{EV} + \mathbf{Z}_{EV}$$

where :

$$\mathbf{X}_{EV} = 0$$

$$\mathbf{Y}_{EV} = (\text{Box to Facet} + \text{Dish Deflection})\cos(\text{Dish Angle}) + (\text{Reflective Radius} + \text{Edge})\sin(\text{Dish Angle})$$

$$\mathbf{Z}_{EV} = (\text{Reflective Radius} + \text{Edge})\cos(\text{Dish Angle}) - (\text{Box to Facet} + \text{Dish Deflection})\sin(\text{Dish Angle})$$

$\mathbf{V}_{OB}$ and $\mathbf{V}_{EV}$ are added to obtain $\mathbf{V}_{OV}$. As shown above the magnitude of $\mathbf{V}_{VT}$ (vertex to target distance can be determined from $\mathbf{V}_{OT}$ and $\mathbf{V}_{OV}$. By substituting into the equation,the value for the vertex to target distance becomes:

$$|V_{EV}| = \sqrt{(X_{OT})^2 + (Y_{OT})^2 + (Z_{OT})^2 + (X_{OV})^2 + (Y_{OV})^2 + (Z_{OV})^2 - 2(X_{OT} * X_{OV} + Y_{OT} * Y_{OV} + Z_{OT} * Z_{OV})}$$

Determining Azimuth Angle

The azimuth angle is determined from the position of the box edge with respect to the ground grid in the x-y plane. The measurements used are all relative to the centerpoint of the grid line.

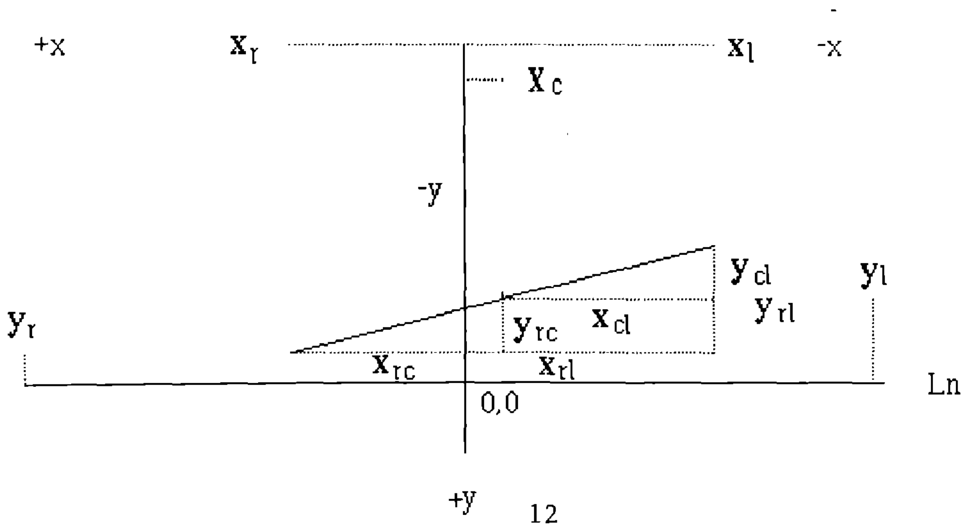

$$x_{rc} = x_r - x_c \quad y_{rc} = y_r - y_c$$

$$x_{cl} = x_c - x_l \quad y_{cl} = y_c - y_l$$

$$x_{rl} = x_r - x_l \quad y_{rl} = y_r - y_l$$

$$\tan(\theta) = \frac{|y_{rc}|}{|x_{rc}|} = \frac{|y_{cl}|}{|x_{cl}|} = \frac{|y_{rl}|}{|x_{rl}|}$$

$$\text{Azimuth angle} = 90^\circ + \theta$$

After each test, a measurement of the vertex-to-target distance was made by stretching a steel cable from the target to the center of the covered facet. This measurement was made to verify the above calculations and did not include any azimuth angle measurement. The table below summarizes these measurements. The maximum difference between the values is 0.2 m. The last three tests do not indicate a design focal length. They were done during the effort to evaluate the 9.5-m focal length discussed in section 5 of the report.

Test Number	Design Focal Length m	Measured Distance m	Calculated Distance m
SAIC			
H0121144	10.5	10.7	10.7
H0121213	10.5	10.5	10.5
H0121224	10.5	10.6	10.6
H0151209	10.0	9.9	10.0
H0151223	10.0	10.0	10.1
H0151232	10.0	10.0	10.0
H0231122	9.5	9.5	9.6
H0231136	9.5	9.4	9.5
H0231148	9.5	9.5	9.5
H0231201	9.5	9.6	9.6
H0231210	9.5	9.6	9.6
H0231218	9.5	9.7	9.7
SKI			
H0251155	10.5	10.3	10.4
H0251205	10.5	10.5	10.6
H0251212	10.5	10.5	10.5
H0251220	10.5	10.6	10.6
H0251228	10.5	10.6	10.7
H0281129	10.0	10.1	10.1
H0301145	10.0	10.3	10.3
H0301154	10.0	10.0	10.0
H0301208	9.5	9.5	9.6
H0301218	9.5	9.5	9.5
H0311031	9.5	na	9.8
H0311039	9.5	na	10.0
H0311049	na	10.4	10.6
H0311109	na	na	9.6
H0311121	na	9.9	10.0

Appendix 2

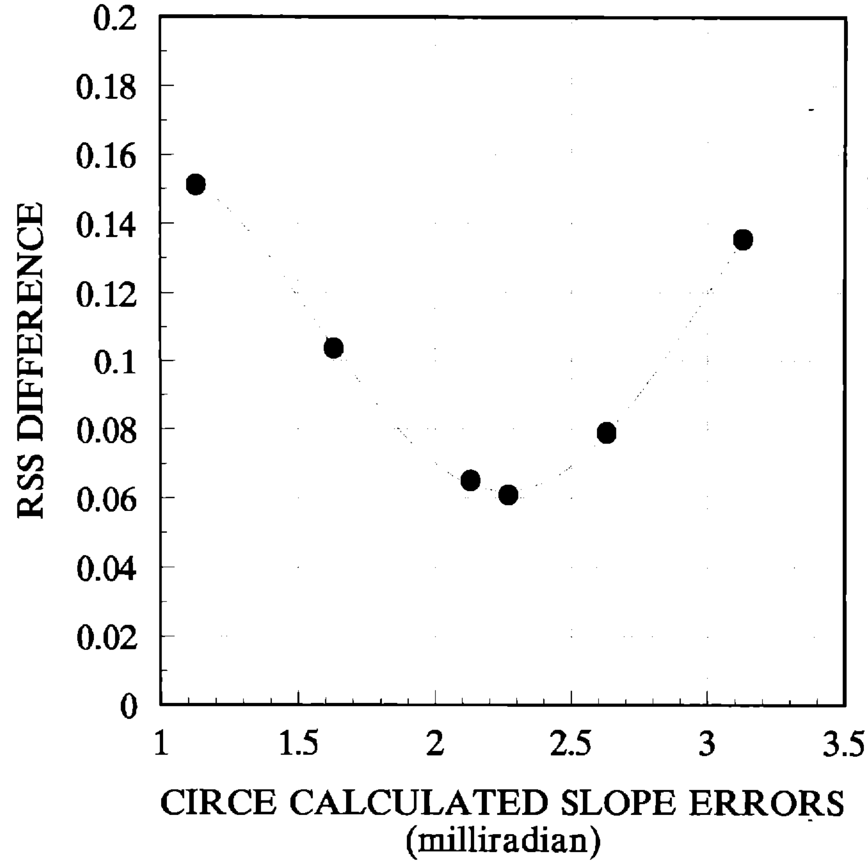

SAIC 10.5 meters
Peak Power 416 kW/sqm
Peak Power Method Slope Error 2.3 mr.
RSS Difference Method Slope Error 2.3 mr.

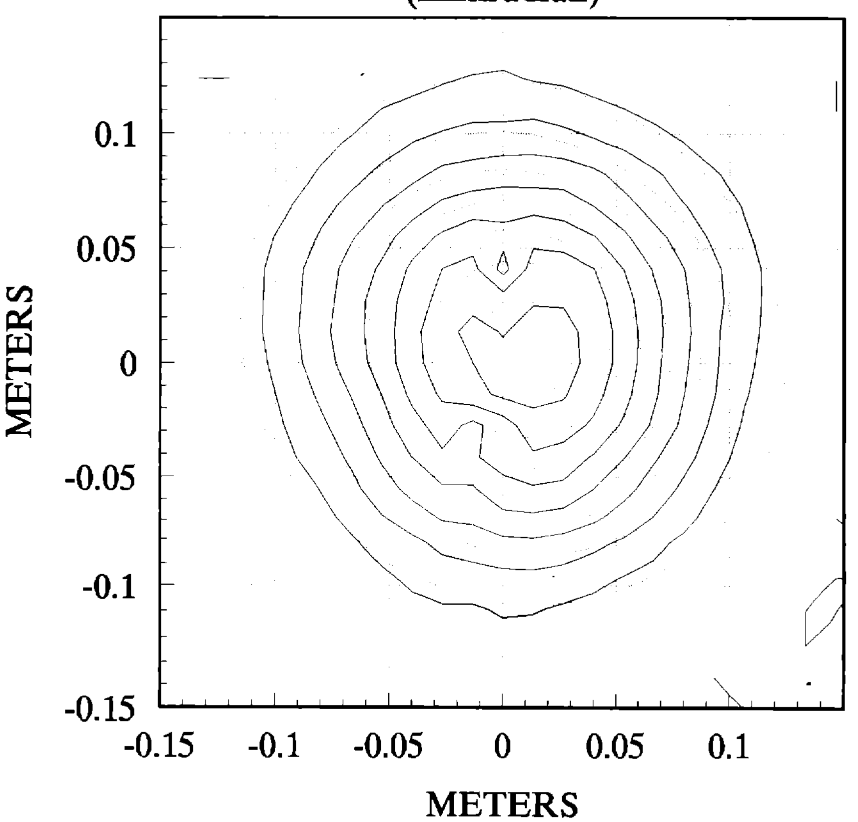

Actual Image
CIRCE2 Prediction

50 Suns/Contour

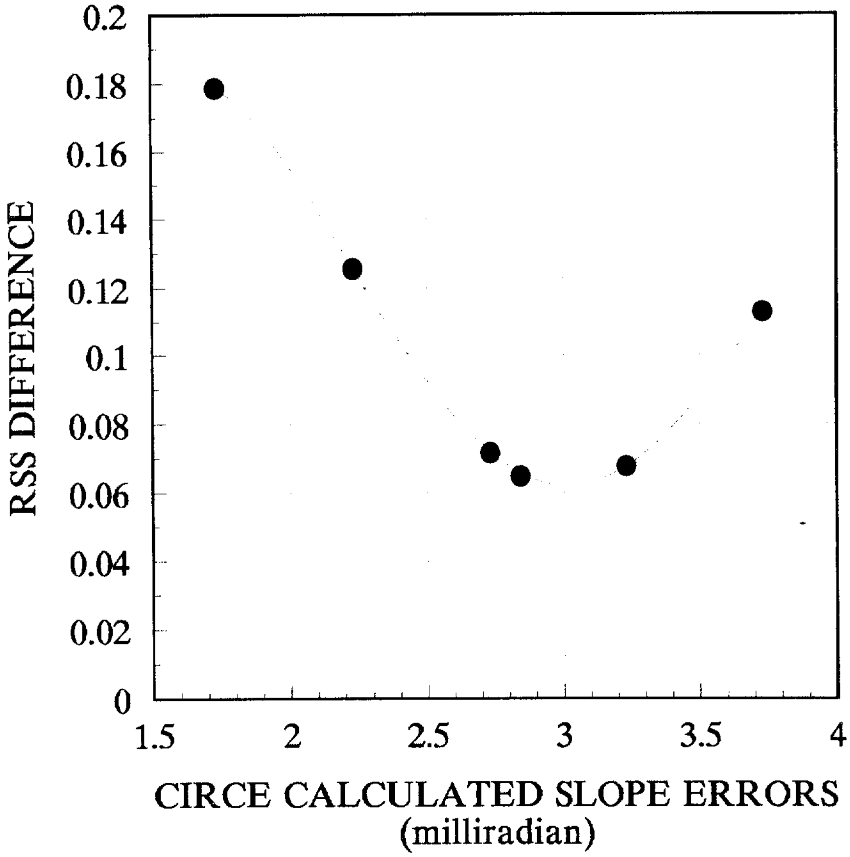

SAIC 10 meters
Peak Power 357 kW/sqm
Peak Power Method Slope Error 2.8 mr.
RSS Difference Method Slope Error 3.0 mr.

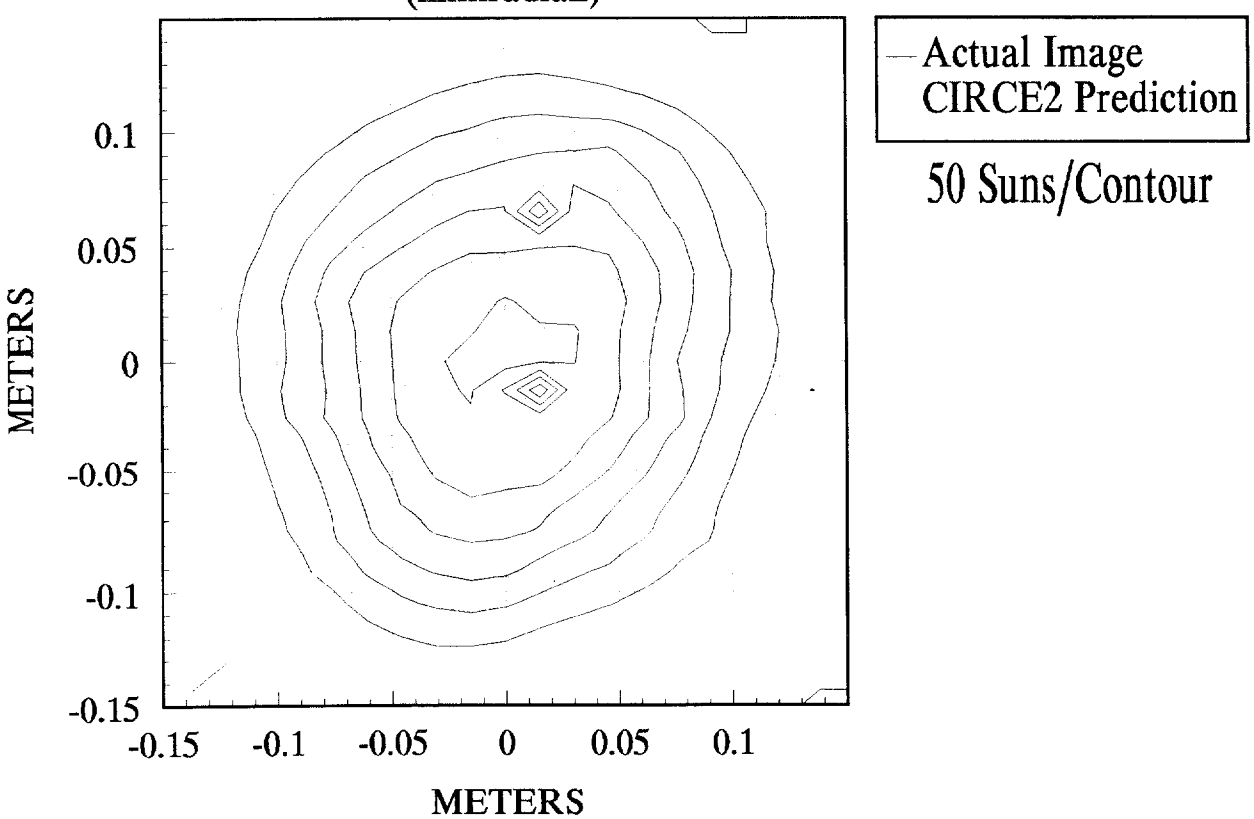

50 Suns/Contour

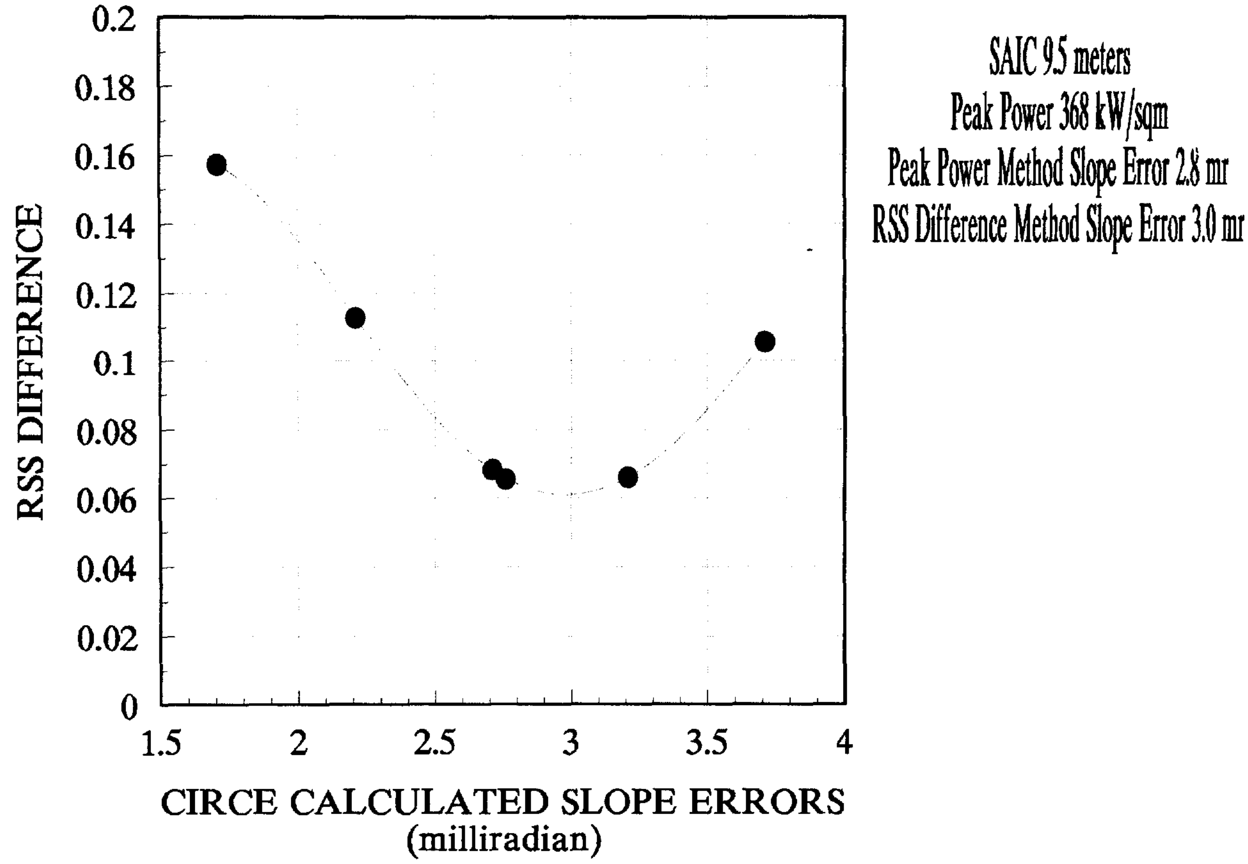
RSS DIFFERENCE
0.2
0.18
0.16
0.14
0.12
0.1
0.08
0.06
0.04
0.02
0
1.5
2
2.5
3
3.5
4
CIRCE CALCULATED SLOPE ERRORS
(milliradian)
SAIC 9.5 meters
Peak Power 368 kW/sqm
Peak Power Method Slope Error 2.8 mr
RSS Difference Method Slope Error 3.0 mr

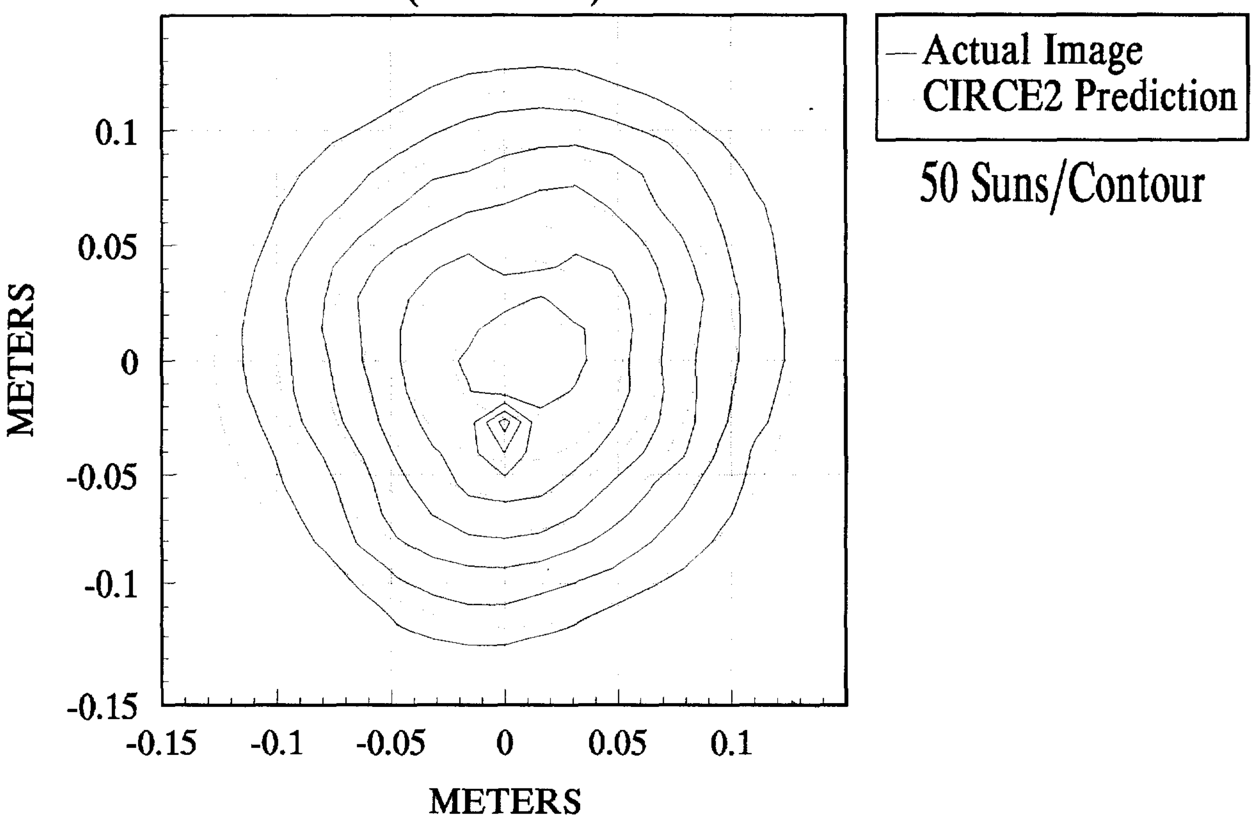
METERS
0.1
0.05
0
-0.05
-0.1
-0.15
-0.15
-0.1
-0.05
0
0.05
0.1
METERS
Actual Image
CIRCE2 Prediction
50 Suns/Contour

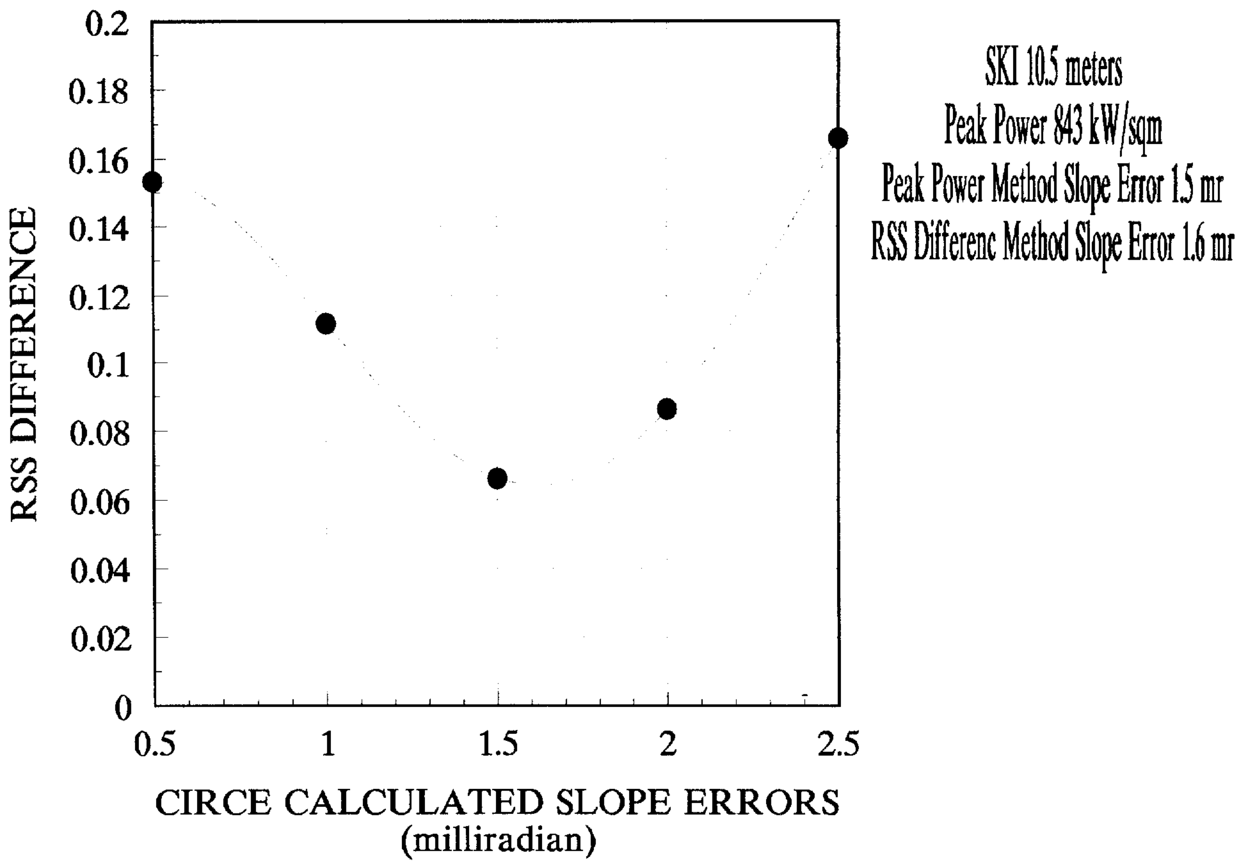

RSS DIFFERENCE
0.2
0.18
0.16
0.14
0.12
0.1
0.08
0.06
0.04
0.02
0
0.5
1
1.5
2
2.5
CIRCE CALCULATED SLOPE ERRORS
(milliradian)
SKI 10.5 meters
Peak Power 843 kW/sqm
Peak Power Method Slope Error 1.5 mr
RSS Differenc Method Slope Error 1.6 mr

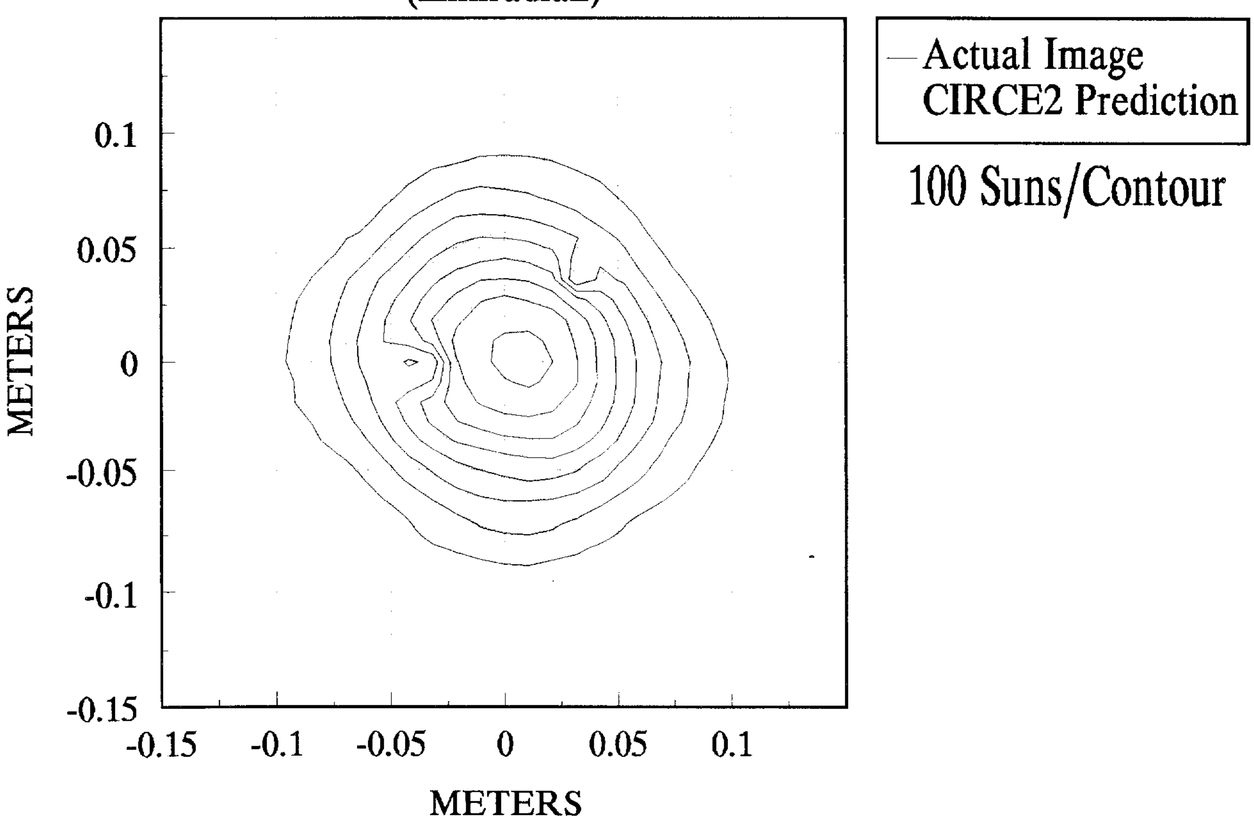

METERS
0.1
0.05
0
-0.05
-0.1
-0.15
-0.15
-0.1
-0.05
0
0.05
0.1
METERS
Actual Image
CIRCE2 Prediction
100 Suns/Contour

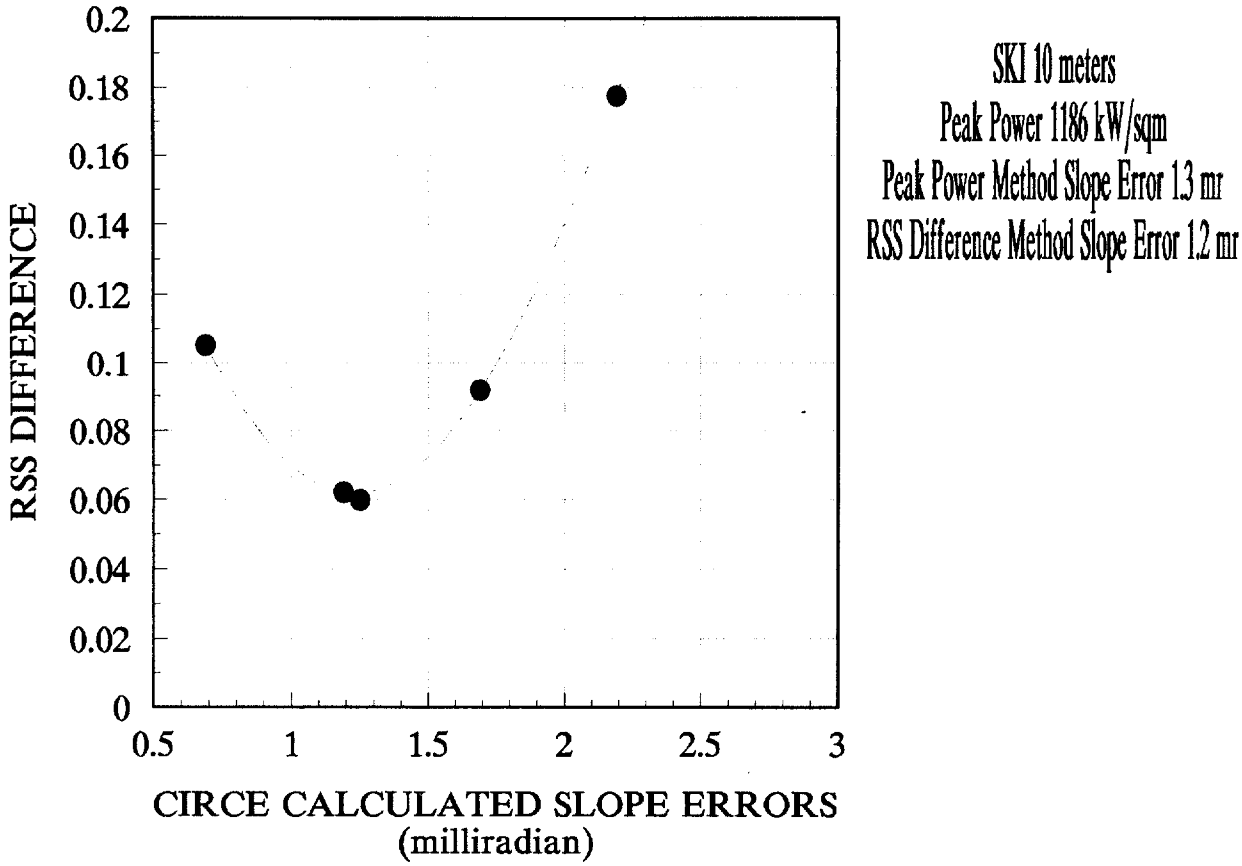
0.2
0.18
0.16
0.14
0.12
0.1
0.08
0.06
0.04
0.02
0
0.5
1
1.5
2
2.5
3
RSS DIFFERENCE
CIRCE CALCULATED SLOPE ERRORS
(milliradian)
SKI 10 meters
Peak Power 1186 kW/sqm
Peak Power Method Slope Error 1.3 mr
RSS Difference Method Slope Error 1.2 mr

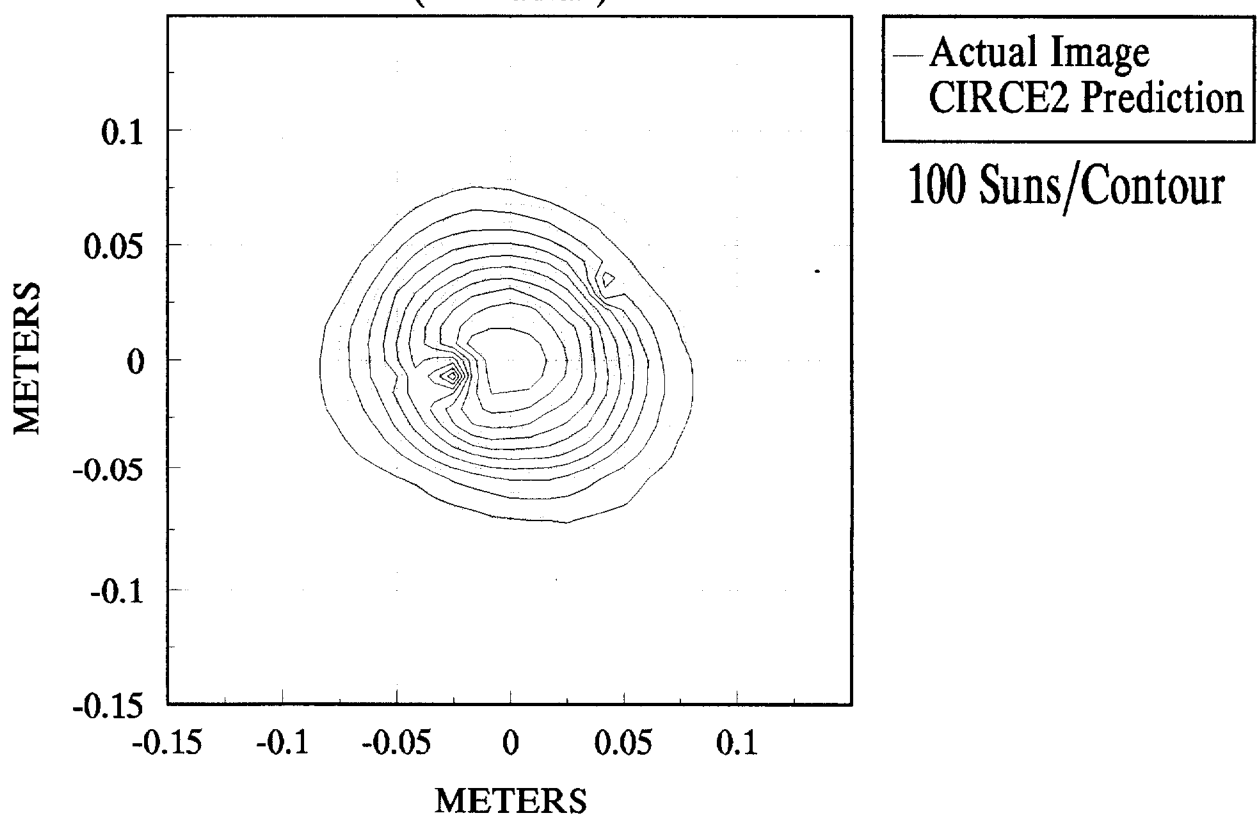
0.1
0.05
0
-0.05
-0.1
-0.15
-0.15
-0.1
-0.05
0
0.05
0.1
METERS
METERS
Actual Image
CIRCE2 Prediction
100 Suns/Contour

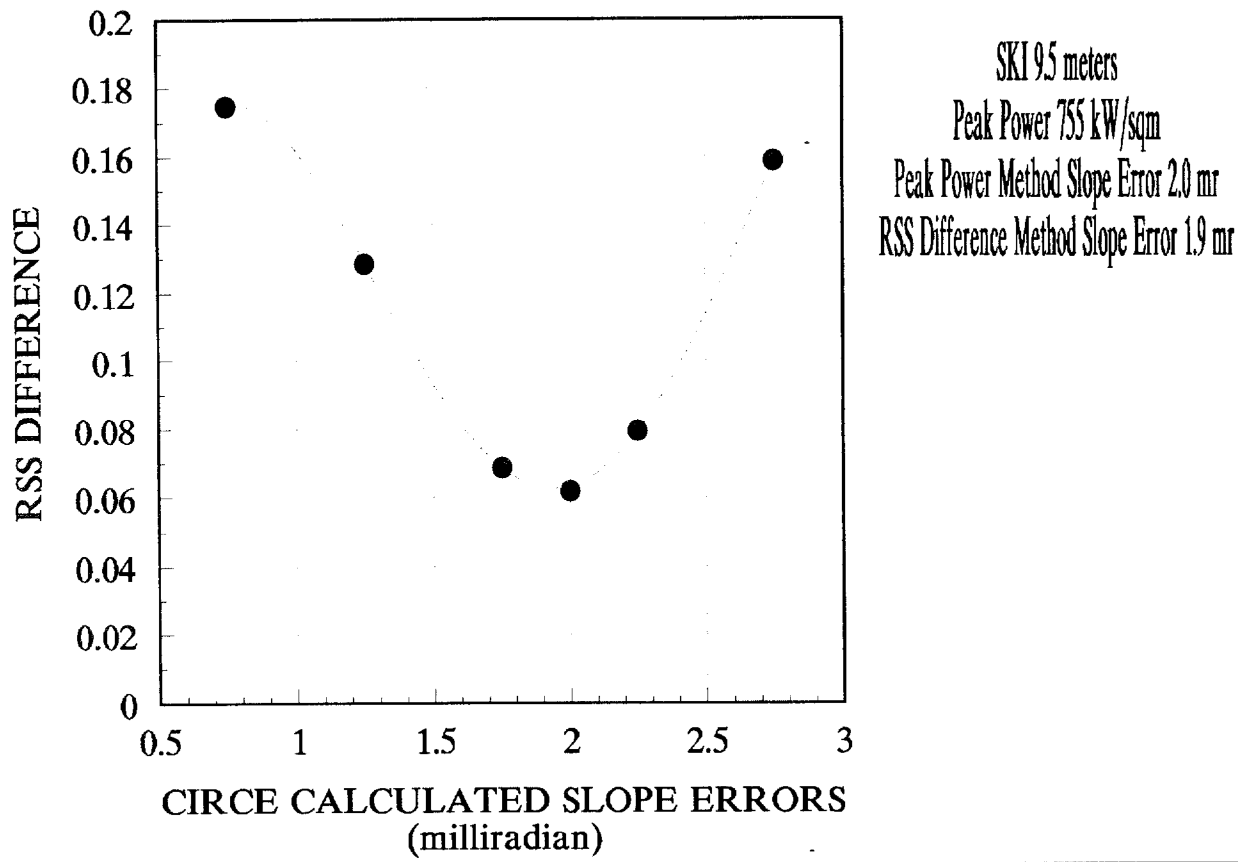

0.2
0.18
0.16
0.14
0.12
0.1
0.08
0.06
0.04
0.02
0
RSS DIFFERENCE
0.5
1
1.5
2
2.5
3
CIRCE CALCULATED SLOPE ERRORS
(milliradian)
SKI 9.5 meters
Peak Power 755 kW/sqm
Peak Power Method Slope Error 2.0 mr
RSS Difference Method Slope Error 1.9 mr

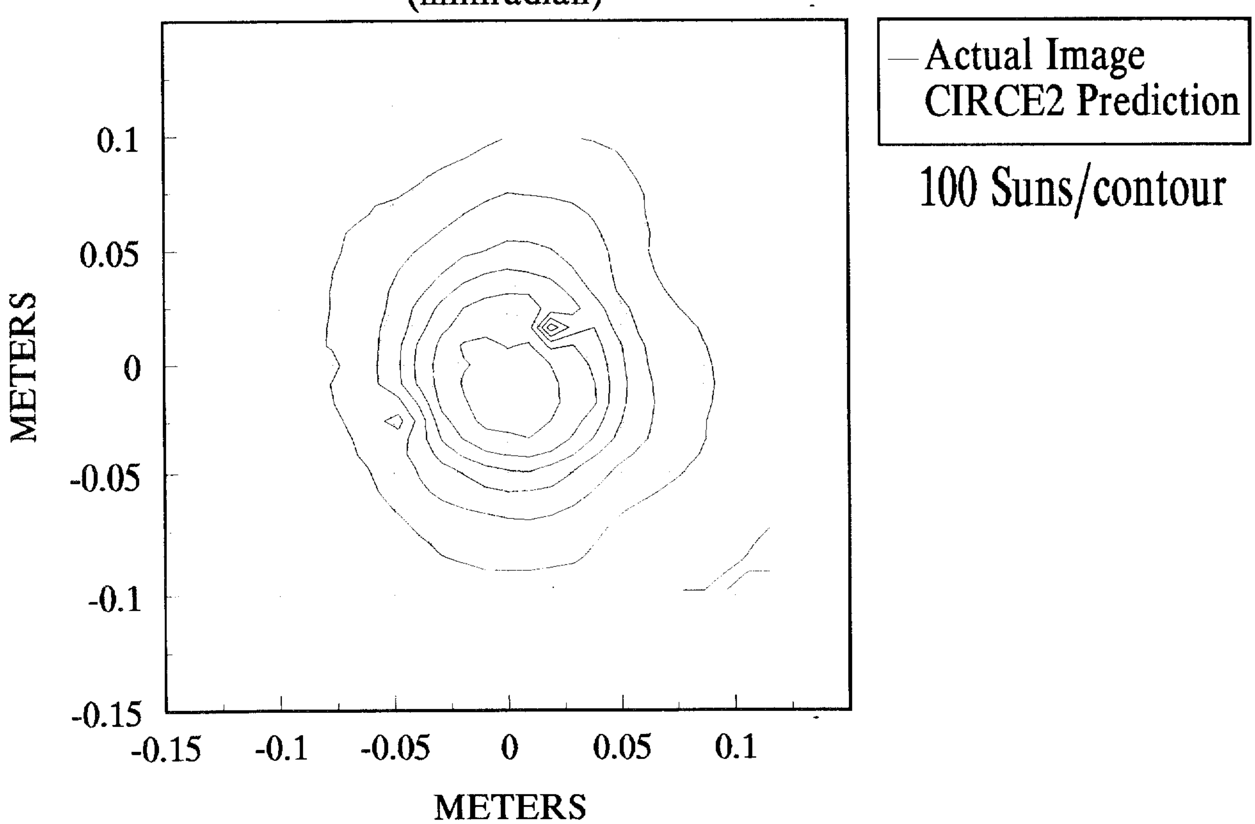

0.1
0.05
0
-0.05
-0.1
-0.15
METERS
-0.15
-0.1
-0.05
0
0.05
0.1
METERS
Actual Image
CIRCE2 Prediction
100 Suns/contour

UNLIMITED DISTRIBUTION
INITIAL DISTRIBUTION
REVISION 12/2/91/jwg

U.S. Department of Energy (4)
Forrestal Building Code
CE-132 1000
Independence Avenue, SW
Washington, DC 20585
Attn: G. Burch
S. Gronich

U.S. Department of Energy (2)
Forrestal Building
Code CE-13
1000 Independence Avenue, SW
Washington, DC 20585
Attn: B. Annan

U.S. Department of Energy
Forrestal Building Code
CE-10
1000 Independence Avenue, SW
Washington, DC 20585
Attn: R. San Martin

U.S. Department of Energy (3)
Albuquerque Operations Office
P.O. Box 5400
Albuquerque,NM 87115
Attn: C. Garcia
G. Tennyson
N. Lackey

U.S. Department of Energy
San Francisco Operations Office
1333 Broadway
Oakland, CA 94612
Attn: R. Hughey

AAI Corporation
P. O. Box 6787
Baltimore, MD 21204

Acurex Corporation (2)
555 Clyde Avenue
Mountain View, CA 94039
Attn: H. Dehne

Advanced Thermal Systems
7600 East Arapahoe
Suite 319 Englewood, CO 80112
Attn: D. Gorman

Allegheny Ludlum Steel
80 Valley Street
Wallingford, CT 06492
Attn: J. Halpin

Analysis Review & Critique
6503 81st Street
Cabin John, MD 20818
Attn: C. LaPorta

Arizona Public Service Company
P.O. Box 53999
M/S 9110
Phoenix,AZ 85072-3999
Attn: W. J. McGuirk

Arizona Solar Energy Office
3800 North Central
Phoenix, AZ 85012
Attn: R. Williamson

Australian National University
Department of Engineering Physics
P. O. Box 4
Canberra ACT 2600 AUSTRALIA
Attn: S. Kaneff

Barber-Nichols Engineering
6325 West 55th Avenue
Arvada, CO 80002
Attn: R. Barber

Battelle Pacific Northwest Laboratory (2)
P.O. Box 999
Richland,WA 99352
Attn: D. Brown

BDM Coporation
1801 Randolph Street
Albuquerque,NM 87106
Attn: W. Schwinkendorf

Bechtel National, Inc.
50 Beale Street
50/15 D8
P. O. Box 3965
San Francisco, CA 94106
Attn: P. DeLaquil

Black & Veatch ConsultingEngineers
P.O. Box 8405
Kansas City, MO 64114
Attn: J. C. Grosskreutz

Tom Brumleve
1512 Northgate Road
Walnut Creek, CA 94598

California Energy Commission
1516 Ninth Street, M-S 43
Sacramento, CA 95814
Attn: A. Jenkins

California Polytechnic University
Dept. of Mechanical Engineering
Pomona, CA 91768
Attn: W. Stine

California Public Utilities Com.
Resource Branch, Room 5198
455 Golden Gate Avenue
San Francisco, CA 94102
Attn: T. Thompson

Cummins Engine Co.
MC 60125
P. O. Box 3005
Columbus, IN 47202-3005
Attn: R. Kubo

Cummins Power Generation,Inc.,South
150 Tanne Hill Drive
Abilene, Texas 79602
Attn: M. McGlaun

Dan Ka
3905 South Mariposa
Englewood, CO 80110
Attn: D. Sallis

DLR
Pfaffenwaldring 38-40
7000 Stuttgart 80
FEDERAL REPUBLIC OF GERMANY
Attn: R. Buck

DLR (2)
Linder Hohe
5000 Koln 90
FEDERAL REPUBLIC OF GERMANY
Attn: M. Becker
M. Bohmer

DSET
P. O. Box 1850
Black Canyon Stage I
Phoenix, AZ 85029
Attn: G. Zerlaut

Electric Power Research Institute
P.O. Box 10412
Palo Alto, CA 94303
Attn: J. Schaeffer

Engineering Perspectives
20 19th Avenue
San Francisco, CA 94121
Attn: John Doyle

Energy Technology Engr. Center
Rockwell International Corp.
P. O. Box 1449
Canoga Park, CA 91304
Attn: W. Bigelow

ENIECH, Inc.
P. O. Box 612246
DFW Airport,TX 75261
Attn: R. Walters

Flachglas Solartechnik GmbH
Muhlengasse7
D-5000 Koln 1
FEDERAL REPUBLIC OF GERMANY
Attn: J. Benemann

Flachglas Solartechnik GmbH
Sonnefistr. 25
D-8000 Munchen 1
FEDERAL REPUBLIC OF GERMANY
Attn: M. Geyer

Florida Solar Energy Center
300 State Road 401
Cape Canaveral, FL 32920
Attn: Library

Ford Aerospace
Ford Road
Newport Beach, CA 92663
Attn: R. Babbe

Foster Wheeler Solar Development
Corporation (2)
12 Peach Tree Hill Road
Livingston, NJ 07039
Attn: M.- Garber
R. Zoschak

Garrett Turbine Engine Co.
111 South 34th Street
P. O. Box 5217
Phoenix, AZ 85010
Attn: E. Strain

Georgia Power (2)
7 Solar Circle
Shenandoah, GA 30265
Attn: W. King

Harris Corporation (2)
Govermnent and Aerospace Systems
Division
P. O. Box 9400
Melbourne, FL 32902
Attn: K. Schumacher

Industrial Solar Technologies
5775 West 52nd Avenue
Denver, CO 80212
Attn: R. Gee

Institute of Gas Technology
34245 State Street
Chicago, IL 60616
Attn: Library

ISEIR
951 Pershing Drive
Silver Spring,MD 20910
Attn: A. Frank

Lawrence Berkeley Laboratory
MS 90-2024
One Cyclotron Road
Berkeley, CA 94720
Attn: A. Hunt

Luz International (2)
924 Westwood Blvd.
Los Angeles, CA 90024
Attn: D. Kearney

3M-Energy Control Products (2)
207-1W 3M Center
St. Paul, MN 55144
Attn: R. Dahlen

Mechanical Technology, Inc. (2)
968 Albany Shaker Road
Latham,NY 12110
Attn: G. Dochat
J. Wagner

Meridian Corporation
4300 King Street
Alexandria,VA 22302
Attn: D. Kumar

NASA Lewis Research Center (4)
21000 Brook Park Road
Cleveland, OH 44135
Attn: R. Corrigan,500-221
L. Greenlee, 500-221
T. Mroz, 301-5
J. Calogeras, 301-5

Nevada Power Co.
P. O. Box 230
Las Vegas, NV 89151
Attn: Mark Shank

NREL (5)
1617 Cole Boulevard
Golden, CO 80401
Attn: T. Williams
L. M. Murphy
G. Jorgensen
T. Wendelin
A. Lewandowski

Pacific Gas and Electric Company (2)
3400 Crow Canyon Road
San Ramon, CA 94526
Attn: G. Braun
J. Iannucci

Peerless Winsmith, Inc.
172 Eaton Street
P. O. Box 530 Springville, NY 14141
Attn: W. Heller

Polydyne, Inc.
1900 S. Norfolk Street, Suite 209
San Mateo, CA 94403
Attn: P. Bos

Power Kinetics, Inc.
415 River Street
Troy,NY 12180-2822
Attn: W. Rogers

Renewable Energy Institute
1001 Connecticut Ave. NW
Suite 719
Washington, DC 20036
Attn: K Porter

Rocketdyne Division
6633 Canoga Park Ave.
Canoga Park,CA 91304
Attn: W. Marlatt

San Diego Gas and Electric Company
P.O. Box 1831
San Diego,CA 92112
Attn: R. Figueroa

SCE
P. O. Box 800
Rosemead, CA 91770
Attn: C. Lopez

Schlaich, Bergennann & Partner
Hohenzollernstr. 1
D - 7000 Stuttgart 1
West Germany
Attn: W. Schiel

Science Applications International
Corporation (2)
10343 Roselle Street, Suite G
San Diego, CA 92121
Attn: K. Beninga
J. Sandubrae

Science Applications International
Corporation
Mail Stop 32
10206 Campus Point Court
San Diego, CA 92121
Attn: B. Butler

Solar Kinetics, Inc. (2)
P.O. Box 540636
Dallas, TX 75354-0636
Attn: J. A. Hutchison
P. Schertz
D. Konnerth

Solar Power Engineering Company
P.O. Box 91
Morrison, CO 80465
Attn: H. Wroton

Solar Steam
P. O. Box 32
Fox Island, WA 98333
Attn: D. Wood

SRS Technologies
990 Explorer Blvd., NW
Huntsville, AL 35806
Attn: R. Bradford

Stearns Catalytic Corporation
P.O. Box 5888
Denver, CO 80217
Attn: T. E. Olson

Stirling Thermal Motors
275 Metty Drive
AnnArbor, MI 48103
Attn: T. Godett

Sun Power, Inc.
6 Byard Street
Athens, OH 45701
Attn: W. Beale

Tom Tracey
6922 South Adams Way
Littleton, CO 80122

United Solar Tech, Inc.
3434 Martin Way
Olympia, WA 98506
Attn: R. Kelley

University of Chicago
Enrico Fermi Institute
5640 Ellis Avenue
Chicago, IL 60637
Attn: J. O'Gallagher

University of Houston
Solar Energy Laboratory
4800 Calhoun
Houston, TX 77704
Attn: L. Vant-Hull

University of Utah
Mechanical and Industrial Engineering
Salt Lake City, UT 84112
Attn: B. Boehm

Eric Weber
302 Caribbean Lane
Phoenix, AZ 85022

WGAssociates
6607 Stonebrook Circle
Dallas, TX 75240
Attn: V. Goldberg

140 R. E. Loehman
1846 D. H. Doughty
1846 C. S. Ashley
3141 S. A. Landenberger (5)
3145 Document Processing (8)
For DOE/OSTI
3151 G. C. Claycomb(3)
4051 Disclosure Division (3)
6000 D. L. Hartley
6200 B. W. Marshall
6215 C. P. Cameron
6215 R. M. Houser
6216 C. E. Tyner
6216 L. Yellowhorse
6216 D. J. Alpert
6216 J. W. Grossman (20)
6216 T. R. Mancini (3)
6216 J. E. Pacheco
6217 P. C. Klimas
6217 R. B. Diver
6220 D. G. Schueler
6221 T. C. Bickel
6221 A. R. Mahoney
6223 G. J. Jones
6224 D. E. Hasti
7470 J. L. Ledman
7476 F. P. Gerstle
7476 S. T. Reed
8523 Central Technical Files